Check for updates

Analysis of Large Eddy Simulations and 1D Hot-Wire Data to Determine Actively Generated Main Flow Turbulence in a Film Cooling Test Rig

Lukas Fischer[1]
Department of Aerospace Engineering,
Institute of Thermodynamics,
Bundeswehr University Munich,
85577 Neubiberg, Germany
e-mail: L.Fischer@unibw.de

Michael Straußwald
Department of Aerospace Engineering,
Institute of Thermodynamics,
Bundeswehr University Munich,
85577 Neubiberg, Germany

Michael Pfitzner
Department of Aerospace Engineering,
Institute of Thermodynamics,
Bundeswehr University Munich,
85577 Neubiberg, Germany

Active turbulence generators were incorporated into a wind tunnel to investigate more realistic inflow conditions for a film cooling test rig. The flow field signals are sampled numerically by probes in large eddy simulations (LES) and experimentally using 1D hot-wire measurements to determine turbulence quantities. The LES shows that the turbulence is anisotropic which cannot be detected by the 1D hot-wire. Furthermore, the integral length scale which shall provide insight into the sizes of the turbulent eddies is determined using two approaches. The first uses the one probe at two times correlation method and could be evaluated from the numerical and experimental probes. The second correlation method exploits the spatial resolution in the LES domain using the two probes at one time approach. Both methods show combustor-like turbulence length scales downstream of the active turbulence generators if the triple decomposition is applied onto the velocity signal. [DOI: 10.1115/1.4054778]

Keywords: computational fluid dynamics (CFD), heat transfer and film cooling

1 Introduction

The performance of jet-engines highly depends on the turbine inlet temperature. Typically, temperatures exceed the allowable material temperature of the components in the combustion chamber and turbine. Thus, film cooling methods are applied to reduce the heat load of these components. Reynolds-averaged Navier–Stokes (RANS) simulations have been applied but results indicated that the steady-state approach is not feasible to properly predict the mean flow field and film cooling effectiveness near the wall [1,2]. However, many optimizations processes use this approach to develop superb film cooling geometries. Sperling et al. [3] showed that the prediction of film cooling effectiveness can be significantly improved using unsteady RANS simulations by considering the dominant frequency from the broadband spectrum of the velocity signal at the inlet upstream of the film cooling injection. This finding emphasizes that the unsteadiness of the inlet boundary conditions are of high importance to predict the correct film cooling effectiveness.

Recent numerical film cooling studies applying large eddy simulations (LES) showed good agreement with experimental data at low turbulence conditions [4–6]. However, in gas turbines, the jets emanating from effusion cooling holes in the combustor or in the turbine are affected by a highly turbulent flow field. How is this field characterized?

Lubbock and Oldfield [7] give an overview of hot rich burn combustor studies from the 1970s to the 1990s and conclude that the turbulence at the combustor exit depends on the geometry, swirl and the mixing process (due to main flow and secondary (dilution) flows) as opposed to the combustion process itself. The turbulence intensity is usually between 10% and 20% for low and high swirlers. For rich burn combustors, measured turbulence length scales are only available from experiments with low swirl combustors and are of the order 10–20 mm (0.4–0.8 in.). The studies focused on the turbulence boundary conditions at the combustor–turbine interface. Only one study gives information of the turbulence quantities in the primary zone [8]. Moreover, it was concluded that rich burn combustors show isotropic turbulence [9]. Note, in the mentioned studies of rich burn combustors, around half of the mass flow enters the main gas path through the combustor liners.

However, in modern lean burn combustors, most of the air enters the main gas path through the fuel injector. There are no mixing jets like in a conventional rich burn combustor. Thus, the fuel injector dominates the combustor exit conditions. Measured turbulence intensity and length scales at the interface were similar to that of rich burn combustors. However, the turbulence length scales in a modern lean burn single-sector combustor were shown to be anisotropic [10,11]. A jet engine representative swirling main flow was created experimentally and numerically [12,13]. The influence of the swirling main flow on a liner with effusion cooling indicated that the generated cooling film is periodically destroyed which reduces the film cooling effectiveness. This further underlines the need of experiments with realistic inflow conditions and unsteady computational fluid dynamics (CFD) simulations because the heat transfer depends on both the turbulence intensity and length scale (see, e.g., Refs. [14,15]). Table 1 summaries the studies which are measured in rich and lean burn combustors and combustor simulators.

In the past, the film cooling experiments at our institute have been conducted at low turbulence levels as well, e.g., Refs. [22,23]. Hence, two turbulence grids were built and tested to increase the mainstream turbulence intensity in the film cooling test section. One of the grids was used for effusion film cooling experiments with higher turbulence intensities in the film cooling test section [24,25]. The quantities of interest which are the turbulence intensity Tu and length scale Λ_1 were determined using 1D hot-wire probes [26].

The aim of this paper is to characterize the created flow fields with respect to gas turbine combustor turbulence by applying 3D large eddy simulations. This way it is possible to sample the

[1]Corresponding author.
Manuscript received November 15, 2021; final manuscript received April 19, 2022; published online July 4, 2022. Tech. Editor: David G. Bogard.

Copyright © 2022 by ASME; reuse license CC-BY 4.0

Downloaded from http://asmedigitalcollection.asme.org/turbomachinery/article-pdf/144/11/111003/6896975/turbo_144_11_111003.pdf by Universitat Der Bundeswehr Munchen user on 08 August 2023

Table 1 Previous studies in rich and lean burn combustors with the turbulence intensity *Tu* and length scale Λ_1

Rich burn references	*Tu* (%)	Λ_1 (mm)
Driscoll and Pelaccio [8]	15–40	18
Moss [16]	9	7
Barringer et al. [17]	15–18	60–120
Cha et al. [18]	20–35	8–17
Lubbock and Oldfield [7]	11–26	7–20
Lean burn references	***Tu* (%)**	**Λ_1 (mm)**
Bacci et al. [19]	15–35	
Koupper et al. [20]	20–22	4.5–9
Schroll et al. [21]	10–20	
Willert et al. [11]		3.75–30
Lenzi et al. [13]	10–75	2–20

created turbulent velocity field upstream of the film cooling test section as well. There is no optical access in the wind tunnel to apply particle image velocimetry (PIV) in a plane perpendicular to the main flow direction upstream of the test section to get these data. Furthermore, the velocity field near the wall using PIV methods may be inaccurate. The sampled velocity boundary conditions enable one to run more realistic film cooling CFD simulations which can be compared to experimental data as well. This paper is organized as follows. The experimental setup is described as well as the hot-wire measurement technique. Subsequently, the numerical approach is given followed by the post-processing of the unsteady velocity field for the CFD and experiment. Then, the LES is validated by the experimental data and the results are discussed.

2 Experimental Setup

Measurements were carried out in a closed-loop wind tunnel facility ("Göttinger" design). The flow in the wind tunnel is driven by a radial fan with a diameter of 1 m (39.4 in.) and a motor power of 69.5 kW. Before reaching the open path test section, a 4:1 contraction nozzle reduces the cross section to 1060 mm × 706 mm (41.7 in. × 28.8 in.). Since the turbulence generators were designed for a thermal wind tunnel facility, the test section of the atmospheric wind tunnel had to be modified to meet the constraints of the thermal wind tunnel. A wooden channel, depicted in Fig. 1, was installed inside the open path test section such that the contraction nozzle of this additional geometry attaches to the inlet. It further reduces the size of the channel to a final flow cross section of 400 × 150 mm (15.8 in. × 5 in.). The turbulence intensity in the test section without a turbulence generator is around 0.5%. The turbulence generators, called vortex generator (VG) and active turbulence grid (ATG), are mounted between two channel segments with constant cross section. The upstream segment has a length of 400 mm (15.8 in.) and the downstream segment has a length of 1000 mm (39.4 in.). The downstream segment can be accessed through hatches in the upper wall and hot-wire probes can be placed inside this segment using optical rails that are mounted at the side walls of the channel. Figure 1 further indicates the location of the origin of the coordinate system in the center of the turbulence generator.

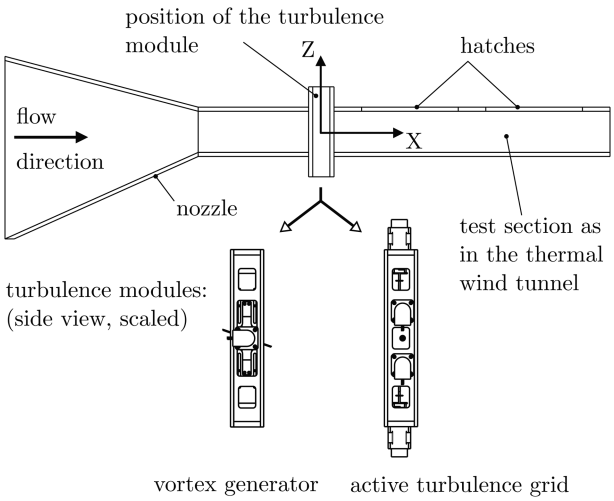

Fig. 1 Test section geometry inside the atmospheric wind tunnel

2.1 Vortex Generator. The vortex generator consists of a single horizontal axis (diameter of 7 mm (0.28 in)) equipped with a flat plate (400 mm × 95 mm × 1.5 mm, 15.8 in. × 3.7 in. × 0.06 in., width × height × thickness) that is mounted through the centerline of the axis (see Fig. 2). The axis is driven by a brushless DC motor (Nanotec, DB42S03). The motor is equipped with a high-torque planetary gear (Nanotec, GP42-S2-15-SR, reduction ratio of 15) to resist the torque which is generated by the rotating plate. The position of the axis can be vertically adjusted to modify the distance of the generated vortices from the surface. The axis was positioned in the center ($Z = 0$). The motor control system (Sigmatek, S-DIAS processor module CP102 and S-DIAS DRIVE-Module DC062 including break resistor) allows three operating conditions: constant plate orientation, constant rotation rate, or alternation between two plate orientations. The orientation of the plate was monitored with a forked photoelectric sensor. Experimentally, rotation rates of 40 and 160 rpm were tested (constant within ±3%) as well as the two operation conditions (rotation and alternation). The constant rotation mode with a rate of 160 rpm was chosen out of simplicity. The higher rotation rate helps to reduce computational costs because the duration of one period is shorter.

2.2 Active Turbulence Grid. The active turbulence grid (Fig. 3) is based on the work of Makita [27] and Makita and Sassa [28] and was redesigned to fit the geometrical constraints of the thermal wind tunnel test section. Three horizontal and eight vertical axes are placed inside the flow cross section forming an evenly spaced grid. Diamond-shaped winglets are mounted onto the axes filling the room around the grid. All axes are driven by brushless DC motors (DB42S03, Nanotec) and individually controlled using optical encoders (WEDL5541-B14, Nanotec), forked photoelectric sensors, and a S-DIAS system (hardware modules CP112 and DC062) of Sigmatek. By rotating the axes, the winglets periodically open and close the remaining flow cross section through the grid which produces additional turbulence. The individual control of the 11 motors allows various operating modes which result in numerous possible flow conditions. In this work, an individual phase shift was applied on each axis to create a nearly constant

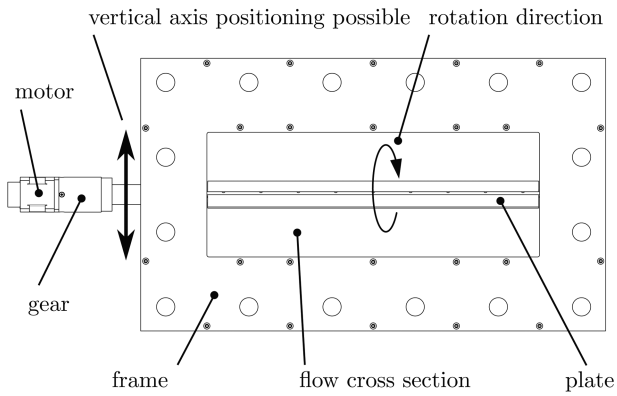

Fig. 2 Vortex generator (looking upstream)

Downloaded from http://asmedigitalcollection.asme.org/turbomachinery/article-pdf/144/11/111003/6896975/turbo_144_11_111003.pdf by Universitat Der Bundeswehr Munchen user on 08 August 2023

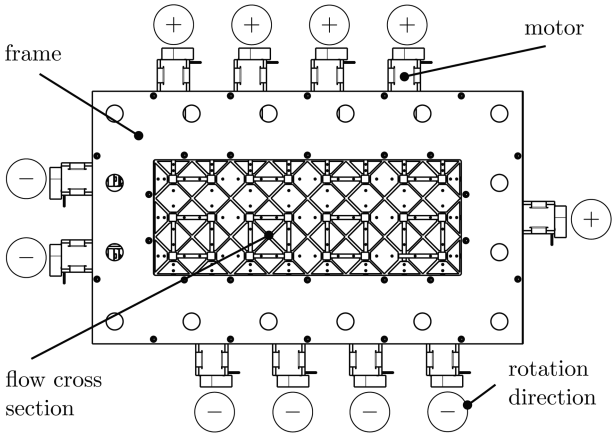

Fig. 3 Active turbulence grid (looking upstream)

blockage of the remaining cross section over time. Rotation rates between 60 and 3600 rpms were tested and 60 rpm was chosen because it creates turbulence quantities similar to the ones in gas turbines. For more details on the investigated parameters, we refer to Ref. [26].

2.3 Measurement Technique. A 1D hot-wire system (Dantec, StreamLine, 90N10 with CTA modules 90C10) was used to measure instantaneous flow velocities. A single wire probe (Dantec, 55P11) was positioned at various locations downstream of the vortex generator using a custom made probe holder and optical rails which are mounted to the side walls inside the test section. A second probe (Dantec, 55P14) was placed upstream ($X = -150$ mm (5.9 in.), $Y = Z = 0$) of the vortex generator to simultaneously measure the unaffected inflow. The probes were calibrated between 0.5 m/s and 50 m/s using an automatic calibration system (Dantec, 90H01 calibration module and 90H02 flow unit). A 2.5 s or 10 s recording period at 20 kHz were chosen for the VG and ATG cases. A sampling frequency of 10 kHz was sufficient to determine converged turbulence time and length scales in a combustor simulator [20].

2.4 Ambient Conditions and Uncertainty. Measurements were carried out at atmospheric conditions. The flow temperature was 20 °C and the static pressure was 960 h Pa, both quantities with an uncertainty well below 1%.

The measurement uncertainty of the single wire probes depends on the turbulence intensity and is given by Bruun [29]. At $Tu = 10\%$, the uncertainty of the average velocity is 0.6% and the uncertainty of the average fluctuation is 0.5%. At $Tu = 30\%$, the uncertainties are increased to 5.0% and 5.7%, respectively. However, actually testing the calibrated hot-wires at several velocities with the automatic calibration flow unit at a turbulence intensity of $Tu \approx 0.0\%$ occasional resulted in an error of the average velocity greater than 3%. Furthermore, the probe location uncertainty was up to 5 mm (0.2 in.) in each direction.

3 Numerical Method

The flow field downstream of the active turbulence generators is expected to be highly turbulent and to have recirculation regions in which the 1D probe may not determine the correct velocity. Hence, 3D LES studies are applied which are conducted with OPENFOAM v1912 using the pressure-based solver "pimpleFoam". This solver has been chosen because of a low Mach number (≤ 0.03) and constant temperature in the simulated part of the wind tunnel section. It has the capability to accommodate moving embedded meshes and compute the correct fluxes accordingly at the mesh interface. The filtered incompressible Navier–Stokes equations are solved. The governing equations are the continuity equation (formulated as a pressure-correction equation)

$$\frac{\partial \tilde{u}_i}{\partial x_i} = 0 \tag{1}$$

and the momentum equations

$$\frac{\partial \tilde{u}_i}{\partial t} + \frac{\partial \tilde{u}_i \tilde{u}_j}{\partial x_j} = -\frac{\partial \tilde{p}}{\partial x_i} + \frac{\partial 2\nu \tilde{S}_{ij}}{\partial x_j} - \frac{\partial \tau_{ij}^{\text{mod}}}{\partial x_j} \tag{2}$$

Filtered variables are denoted by tilde, $\tilde{S}_{ij}$ is the resolved rate-of-strain tensor, and the subgrid stress term τ_{ij}^{mod} accounts for effects from unresolved scales. The chosen subgrid model for the unresolved scales is the wall-adapting local eddy-viscosity model. Due to the size of the domain and the moving mesh, the Spalding wall function implemented in OPENFOAM is used. The equation system is solved with the iterative PISO-SIMPLE (PIMPLE) algorithm with two SIMPLE iterations, two pressure corrections, and one non-orthogonal corrector loop. The initial residuals of the fundamental equations can be reduced by several orders of magnitude using more than one SIMPLE iteration with no under-relaxation. The Green-Gauss-based method and second-order linear interpolation are used for all gradient calculations on the cell faces. The advective term for the velocity field is discretized with a second-order upwind biased scheme to prevent the introduction of velocity oscillations at the interpolation planes between the moving and stationary meshes. Second-order Gaussian quadrature for element face integration, linear interpolation of the diffusion coefficient, and the corrected scheme for the surface normal gradients are used to describe diffusive terms. All cases are run with a second-order implicit discretization in time (Euler backward). Due to the relatively long duration of one rotation period, the physical time-step of the simulations is chosen to allow for a maximum Courant number of 0.9 ($dt \approx 5 \times 10^{-06}$ s). Downstream of the generators where the probes are evaluated, the average Courant number is of order 0.01.

3.1 Computational Domain and Grid. The computational domain consists of a section from the wind tunnel experiments rejecting the upstream nozzle and is depicted in Fig. 4 containing the vortex generator. The coordinates are non-dimensionalized by the rounded plate length $\tilde{L}_p \approx 100$ mm (3.94 in.) of the vortex

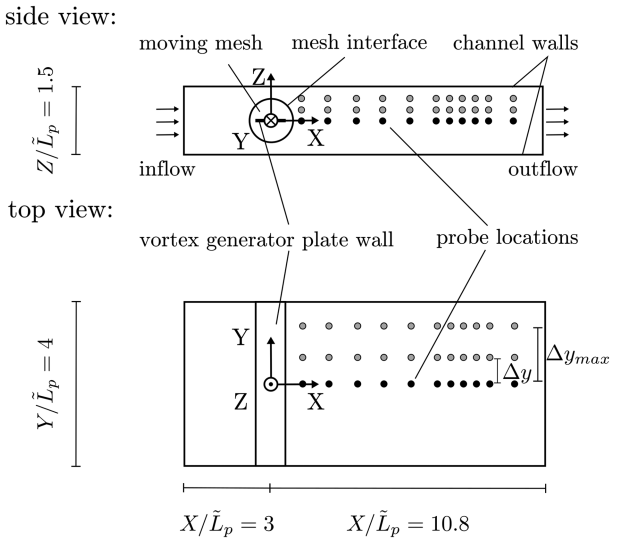

Fig. 4 Sketch of the 3D computational domain including the vortex generator, boundary conditions, and probe locations

Downloaded from http://asmedigitalcollection.asme.org/turbomachinery/article-pdf/144/11/111003/6896975/turbo_144_11_111003.pdf by Universitat Der Bundeswehr Munchen user on 08 August 2023

generator. The origin of the Cartesian coordinate system is located in the center of the turbulence generator module.

The inlet is located three plate dimensions upstream and the other sizes correspond to the actual wind tunnel (Fig. 1). The width of the CFD domain does not account for the optical rails that are mounted at the side walls of the channel. Hence, the CFD does not account for 3D effects resulting from these geometry features. The geometry of the vortex generator is very simple and a block structured meshing approach of the stationary wind tunnel domain and rotating plate domain was chosen. The geometry of the active turbulence generator is more complex and an unstructured meshing approach of the turbulence generator is chosen. The 59 rotating wing domains are placed into a stationary domain to create the mesh for the turbulence generator. Adjacent to this domain, block structured meshes are used to create the mesh for the upstream and downstream sections of the wind tunnel. The unstructured domains are only discretized by tetrahedral cells because the usage of prism layers resulted in low quality elements. However, cell faces perpendicular to the wall are important for the correct usage of wall functions [30] which is not given by the tetrahedral elements. Nevertheless, using only tetrahedral cells is a common approach for complex geometries like, for example, in swirl burners [20,31]. The meshes are created with ANSYS ICEM CFD. Afterwards, the single meshes are converted to the unstructured mesh format of OPENFOAM and merged. Figure 5 shows the grids of both generators near the mesh interfaces.

3.2 Boundary and Initial Conditions. The boundary conditions are visualized in the side view of Fig. 4. The outlet backflow is prevented by setting the reverse velocity to $\vec{0}$ at the patch. The no-slip condition is applied on the walls of the rectangular channel. The velocity distribution along the rotating walls follows the distribution $v_{\text{wall}} = 2\pi \cdot r \cdot \omega$, in which r is the distance from the origin of rotation to the corresponding point on the rotating wall and ω is the rotational speed of the shaft(s) (160 rpm for the vortex generator and 60 rpm for the active turbulence grid). The cyclic arbitrary mesh interface handles non-conformal interfaces in the domain.

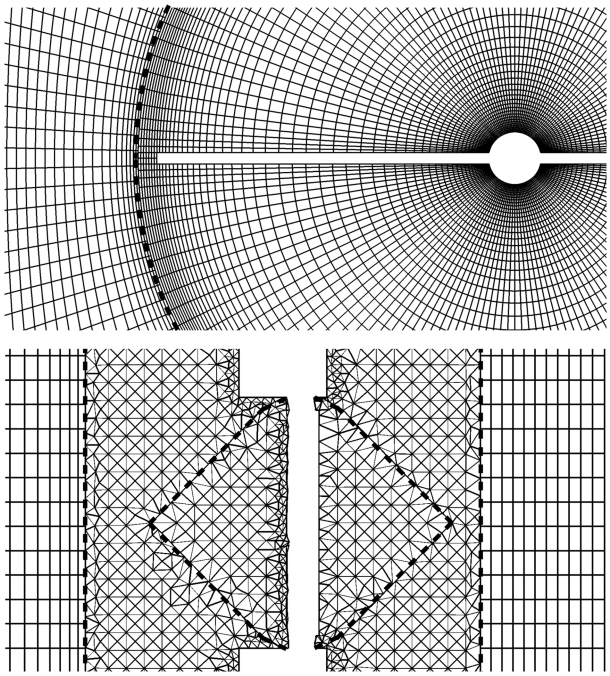

Fig. 5 Computational grid and the interfaces marked by the dashed lines (- - -). Top: vortex generator. Bottom: active turbulence grid.

The velocity inflow condition between the ATG and VG differs and both simulations are started from quiescent air. The plate of the vortex generator is positioned horizontally (lowest blockage of the wind tunnels cross section). The fan of the wind tunnel is operating at constant speed. Thus, the rotating of the plate throttles the fan periodically. A sine function

$$u(t) = \sin(2\pi f(t - t_0))u_{\text{scale}} + \overline{u} \tag{3}$$

describes this behavior of the axial velocity $u(t)$ at the inlet of the domain. The frequency f is twice the rotational speed of the plate (because of the plate's symmetry), in which t is the local time-step, t_0 is the temporal offset, $u_{\text{scale}} = 4.167$ m/s is the velocity to scale the mean axial velocity $\overline{u} = 12.751$ m/s.

The active turbulence grid is operated in a constant blockage mode and Fig. 6 shows the front view of the ATG (for CFD and experiment) and the position of the shafts at one instantaneous moment. The velocity signal of an upstream located hot-wire probe shows a visible rotating frequency of 60 rpm in the frequency spectrum but this only leads to an inflow turbulence intensity of around 2.3%. This indicates that the throttling effect due to the wing rotation may be negligible during constant blockage mode. Thus, a constant inflow velocity upstream of the active turbulence grid of $u_\infty = 7.5$ m/s is set which is determined from the time average probe velocity signal from the upstream hot-wire. All in all, the inlet boundary conditions are in good agreement with the experimental setup.

3.3 Numerical Point Probes. There are numerical point probes in the domain to sample the three velocity components at the same locations of the hot-wire measurements. Additional numerical probes have been placed in the domain to improve the spatial resolution. The data are sampled at 20 kHz equally to the experimental data. Each LES of the VG cases are run for 10 rotation periods (≈ 1.9 s). The first two periods (approximately three through flows of the domain) of the probe signals are skipped to prevent the signal to be corrupted by the initial solution. Hence, eight periods can be used for the signal analyses (≈ 1.5 s). The cases of the ATG followed a similar routine but only seven periods are kept for signal analyses. To allow for a comparison of the numerical and hot-wire data, the numerical probe signal has to be converted to the effective velocity measured by the 1D hot-wire probe. One has to consider that 1D hot-wire probes do not measure one velocity component exclusively. Since the cooling of the probe wire is driven by all three velocity components, the effective velocity v_{eff} follows the equation:

$$v_{\text{eff}} = \sqrt{u^2 + k^2 v^2 + h^2 w^2} \tag{4}$$

in which k and h are pitch factors. Those factors weight the influence of the non-main flow velocity components v and w relative to the main flow component u. While v is aligned parallel with the wire and therefore considered to have a low effect on the cooling of the hot-wire ($k = 0.1$), the third component w is aligned perpendicular to the wire and thus has an equal effect ($h = 1$) as

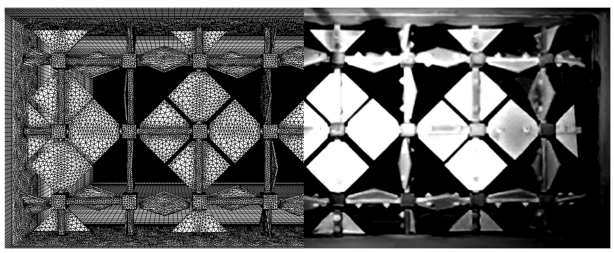

Fig. 6 Instantaneous view of the active turbulence grid operating in constant blockage mode looking upstream. Left: CFD. Right: experiment.

Downloaded from http://asmedigitalcollection.asme.org/turbomachinery/article-pdf/144/11/111003/6896975/turbo_144_11_111003.pdf by Universitat Der Bundeswehr Munchen user on 08 August 2023

the main flow component [29,32]. Since 1D hot-wire data do not allow to derive single velocity components, the numerical data have to be transformed into a hot-wire equivalent signal using Eq. (4) for validation purposes.

4 Post-Processing of Unsteady Velocity Field

The velocity signals $V(t)$ of the probes are post-processed to determine the turbulence quantities of interest. A cross-correlation function was used to determine the time lag between the experimental and CFD signals. Subsequently, both signals are in phase with the same signal length. Usually, the Reynolds decomposition

$$V(t) = V'(t) + \overline{V} \tag{5}$$

is applied to extract the stochastic fluctuation $V'(t)$ of the velocity signal. However, velocity fluctuations investigated in this study contain both the turbulent $V'_s(t)$ and the coherent (periodic) $V'_p(\phi(t))$ part induced periodically by one of the turbulence generators. Hence, only the triple decomposition [33] is applied

$$V(t) = V'_s(t) + V'_p(\phi(t)) + \overline{V} \tag{6}$$

The periodic part depends on the phase angle $\phi(t)$ which is known (rotation speed of the shafts). This allows to determine the periodic fluctuation at a certain phase

$$V'_p(\phi(t_0)) = \lim_{N\to\infty} \frac{1}{N} \sum_{n=0}^{N-1} V(t_0 + nT) - \overline{V} \tag{7}$$

in which T denotes the duration of one (rotation) period and N equals to the number of periods in the signal $V(t)$. The triple decomposition requires averaging over as many periods as possible to calculate a well averaged phase depending fluctuation $V'_p(\phi(t))$ which is numerically not always feasible. Other methods to triple decompose a fluctuating field are described in Ref. [34]. The triple decomposition may also be applied if the fluctuation of the velocity is forced which as well occurs downstream of a rotor in a compressor or turbine.

In the following, the definitions of the turbulence intensity and integral length scale for the one- and two-point approaches are given. The definitions are then applied to the triple decomposed fluctuation V'_s which is referred to as V' in the following.

4.1 Turbulence Intensity.

The isotropic turbulence intensity Tu is defined as

$$Tu = \frac{\sqrt{\overline{V'^2}}}{\sqrt{\overline{u}^2 + \overline{v}^2 + \overline{w}^2}} \tag{8}$$

in which $\sqrt{\overline{V'^2}} = V_{\text{rms}}$ is the mean velocity fluctuation. The velocity component V indicates one of the following components, e.g., u, v, w or the effective velocity v_{eff}.

4.2 Integral Length Scale: One-Point Approach.

The integral length scale can be determined [35–37] by one probe at a fixed location ($\vec{x_0}$) from the correlation coefficient $R_{V'V'}$ of the autocorrelation function with time lag τ:

$$R_{V'V'}(\vec{x_0}, \tau) = \frac{\overline{V'(\vec{x_0}, t)V'(\vec{x_0}, t+\tau)}}{\overline{V'(\vec{x_0}, t)^2}} \tag{9}$$

The overline denotes a time-averaged value. Hence, the time average for each temporal offset τ is computed. One can integrate the coefficient $R_{V'V'}$ up to a certain temporal offset τ^* to determine the integral time scale Λ_τ

$$\Lambda_\tau = \int_0^{\tau^*} R_{V'V'}(\vec{x_0}, \tau)\, \mathrm{d}\tau \tag{10}$$

It quantifies the time interval over which significant correlation persists and returns a measure of the largest turbulent eddies passing this point. The references mentioned in Table 2 used this one-point approach to determine turbulence time scales. Moreover, the integration limit τ^* differs between the whole temporal range $\lim_{\tau^*\to\infty}$ or at which the value of τ^* corresponds to τ at the first zero-crossing of the correlation coefficient $R_{V'V'}(\vec{x_0}, \tau^*) = 0$ or where $R_{V'V'}(\vec{x_0}, \tau^*)$ has a value of 0.5. Which integration limit is a good choice? Koupper et al. [20] varied the integration threshold τ^* between $R_{V'V'}(\vec{x_0}, \tau^*) = 0 - 0.95$ showing that the integral time scale increases with increasing τ^*. However, this depends on the case-specific trend of the correlation coefficient. Figure 7 shows two exemplary correlation coefficients from the vortex generator investigation. If there is no zero-crossing in the considered time frame, integrating over the whole time range would result in very large integral time scales. However, the integral time scale is supposed to characterize the duration of persistently high correlation and choosing $\lim_{\tau^*\to\infty}$ would determine an integral time scale which is more likely to be characterized by low correlation values. Furthermore, other correlation functions tend to have an oscillating "tail" (see, e.g., also Ref. [38]) resulting in a delayed zero-crossing which in turn increases the integral value.

Applying the Taylor's hypothesis (Taylor's frozen turbulence) allows to determine the integral length scale Λ_1

$$\Lambda_1 = \Lambda_\tau \cdot \overline{V} \tag{11}$$

by multiplying the mean convection velocity $\overline{V}$ with the integral time scale. Hence, a length scale only in the mainstream direction can be determined. This definition is actually only valid for

Table 2 Integration limit of the correlation coefficient $R_{V'V'}(\vec{x_0}, \tau)$ for the one-point approach of previous studies in rich and lean burn combustors

References	Integration limit
Driscoll and Pelaccio [8]	$\lim_{\tau^*\to\infty}$
Moss [16]	$R_{V'V'}(\vec{x_0}, \tau^*) = 0$
Barringer et al. [17]	n/a
Cha et al. [18]	$R_{V'V'}(\vec{x_0}, \tau^*) = 0$
Koupper et al. [20]	$R_{V'V'}(\vec{x_0}, \tau^*) = 0.5$
Lubbock and Oldfield [7]	$R_{V'V'}(\vec{x_0}, \tau^*) = 0$
Willert et al. [11]	$\lim_{\tau^*\to\infty}$
Lenzi et al. [13]	n/a

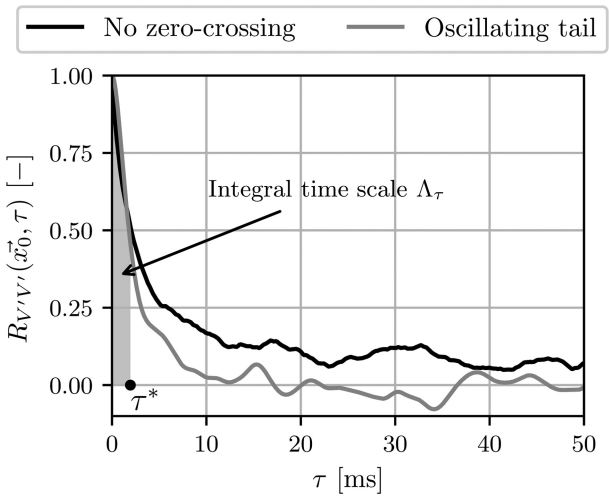

Fig. 7 Overview of two different correlation functions as well as the choice for the integration limit τ^* and the resulting integral time scale Λ_τ, adapted from Ref. [20]

Downloaded from http://asmedigitalcollection.asme.org/turbomachinery/article-pdf/144/11/111003/6896975/turbo_144_11_111003.pdf by Universitat Der Bundeswehr Munchen user on 08 August 2023

conditions $V' \ll \overline{V}$ which is not satisfied downstream of our turbulence generators (and in gas turbine combustors). Moreover, these equations show that it is necessary to use as many signal periods as possible to determine well averaged values for $\overline{V}$ and Λ_τ. If only two signal periods are evaluated, the determined length scale can vary up to 40% depending on which time interval was chosen. Hence, seven (ATG) and eight (VG) periods are evaluated of the experimental and numerical signal leading to a variation of the determined length scale below 5%. A more thorough investigation was necessary for Ref. [20] because the signal length of the numerical data was much shorter than the experimental data which lead to an uncertainty of ±20%. Figure 8 shows the value of the determined turbulence length scale Λ_1 as a function of the integration limit for the correlation coefficient $R_{V'V'}$. Here, the trend upstream of the film cooling test section is shown using generated turbulence from the vortex generator and active turbulence grid. The value of the length scale shows linear trends between integration limits of 0.95–0.7 and 0.65–0.25. The estimated sizes of the length scales vary between 2 and 32 mm for the VG and between 2 and 45 for the ATG. In this investigation, an integration limit for τ^* is chosen so that $R_{V'V'}(\vec{x_0}, \tau^*) = 0.5$ (visualized in Fig. 7). This choice is less sensible to oscillating tails of the correlation function which occurs for low integration limits smaller than 0.25. All in all, the size of length scale generated fits into the gas turbine context as shown in Table 1. In addition, one should determine the ratio of the integral length scale to the used film cooling diameter (Λ_1/D) which is done in the final section of this work.

4.3 Integral Length Scale: Two-Point Approach. For higher accuracy, the integral length scale can be directly determined using several probes spaced evenly apart by $\Delta\vec{x}$ in, for example, the axial, lateral, or vertical direction [36]. This is referred to as the two-point one time approach. In the numerical domain, the spatial resolution of the probes is much higher than in the experiment. This way it is possible to calculate the correlation coefficient $R_{V'V'}$ as a function of the probe distances (e.g., in axial direction) Δx:

$$R_{V'V'}(\vec{x_0}, \Delta x) = \frac{\overline{V'(\vec{x}, t)V'(\vec{x} + \Delta x, t)}}{\overline{V'(\vec{x}, t)^2}} \tag{12}$$

The (longitudinal) correlation coefficient is evaluated such that the vector of the probe spacing (e.g., Δz) and the velocity component (e.g., $V = w$) are parallel. The integral length scale Λ_2 can be determined by integrating this coefficient in the direction of the probe locations:

$$\Lambda_{2,x} = \int_0^{\Delta x^*} R_{V'V'}(\vec{x_0}, \Delta x)\, dX \tag{13}$$

This way length scales in the X, Y, and Z direction are calculated. The integration limit Δx^* is the distance at which the correlation coefficient $R_{V'V'}(\vec{x_0}, \Delta x) = 0.5$. The maximum spatial probe offset value is chosen to be $\Delta x_{max}/\tilde{L}_p = 1$, $\Delta y_{max}/\tilde{L}_p = 0.1$, and $\Delta z_{max}/\tilde{L}_p = 0.07$ and is schematically depicted for the y direction in Fig. 4. The integration limit Δx^* to reach a value of 0.5 for the correlation coefficient is smaller than Δx_{max}.

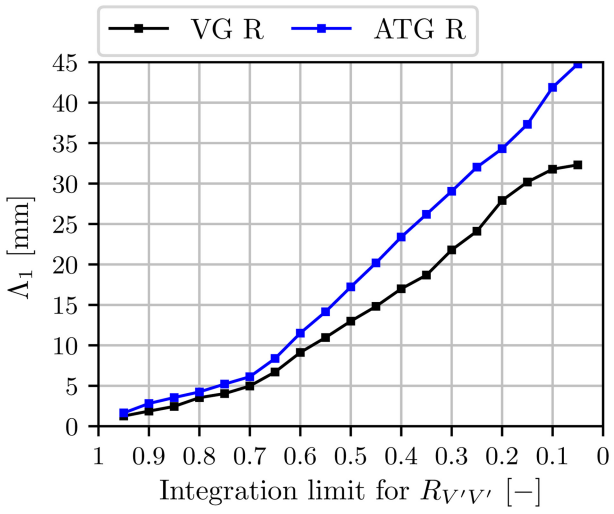

Fig. 8 Influence of the integration limit for $R_{V'V'}$ on the integral length scale Λ_1 upstream of the film cooling test section, adapted from Ref. [20]

5 Mesh Study

For the mesh study of the vortex generator, three meshes are tested comprising of 2 million (coarse), 3 million (medium), and 4.3 million (fine) hexahedral elements. Meshes with more elements are not investigated because the speedup of the parallelization is strongly limited using the moving mesh approach. The fine mesh is based on the medium mesh but is refined in a centered region downstream of the vortex generator by halving the cells in each direction. Numerical probes are placed in cells in which the cubic root of the cell volume is around 2 and 3 mm (0.08 and 0.12 in.) for the fine and medium case. The ratio of the turbulent kinetic energy k_{res} to the total turbulent kinetic energy $k_{res} + \overline{k}_{sgs}$, with $\overline{k}_{sgs}$ being the time-averaged subgrid turbulent kinetic energy higher than 85% throughout the domain (medium mesh). Pope [36] estimates that 80% are needed for an LES simulation with near-wall resolution. Reducing the time-step by half (maximum Courant number of 0.45) on the finest mesh did not lead to a different solution. Additionally, a simple mesh was created which only consists of the part downstream of the moving mesh. The velocity field downstream of the turbulence generator is sampled (medium case) and can be recycled as the inlet boundary condition for the simple mesh. The reconstruction of a sampled velocity field was successfully applied in Ref. [31], as well. This allows for a mesh with a higher resolution and a computational speedup because the parallelization is not as limited as by using a moving mesh. This mesh is based on the part downstream of the moving mesh containing 4× more cells. Afterwards, it was refined in a centered region leading to 32× more cells in the region of interest with respect to the medium mesh. The numerical settings were adjusted to this fully orthogonal mesh and central differencing schemes for the divergence terms were applied. In the following, this solution is referred to the recycled CFD (CFD R) solution.

Figure 9 depicts the trend of the turbulence intensity Tu and of the integral length scale Λ_1 along the centerline of the wind tunnel. The velocity vector of the numerical probes was converted to the measured hot-wire velocity v_{eff} using Eq. (4). All meshes show that the turbulence intensity decreases downstream of the vortex generator and the integral length scale increases downstream of the vortex generator. The difference of turbulence intensity Tu between the medium and fine mesh is small at low and high $X/\tilde{L}$. The recycled CFD solution shows increased turbulence intensity which may be due to the usage of pure central differencing schemes in contrast to the second-order upwind biased schemes. However, at the film cooling location $X/\tilde{L} \approx 7$ the turbulence intensity differs by only 1%. The integral length scale using the one-point approach is strongly affected by the mesh resolution. There is mesh independence visible for the integral length scale between the fine and recycled CFD solution. The medium mesh overestimates the length scale by around 5 mm (0.2 in.). Based on the shown mesh independence, a medium mesh was created for the ATG as well as a high resolved simple mesh for recycling purposes to reduce the computational effort.

Downloaded from http://asmedigitalcollection.asme.org/turbomachinery/article-pdf/144/11/111003/6896975/turbo_144_11_111003.pdf by Universitat Der Bundeswehr Munchen user on 08 August 2023

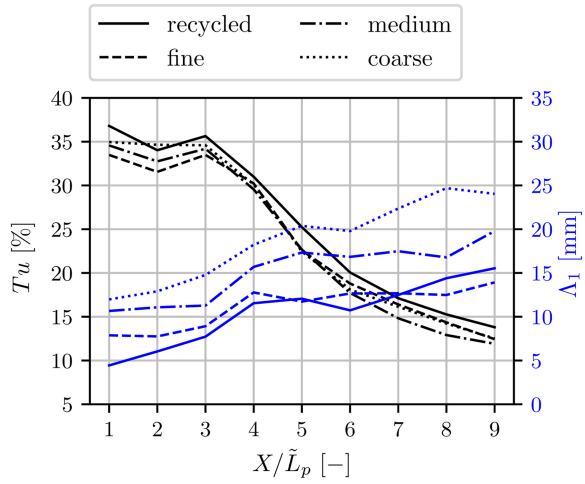

Fig. 9 VG: mesh study for turbulence intensity *Tu* (black lines) and Taylor macro-scale Λ_1 (gray lines) along the centerline using the hot-wire converted velocity signal v_{eff}

6 Validation of Large Eddy Simulations Data

The 1D hot-wire data are employed to validate against the converted signals of the LES probes (v_{eff}). The frequency spectra at $X/\tilde{L}_p = 1$ of the experimental and numerical probe signals are shown in Fig. 10. The LES simulation on the fine mesh is able to resolve turbulence fluctuations without noticeable damping for frequencies of up to 800 Hz. The medium mesh resolves frequencies up to 400 Hz (not shown). The hot-wire experiment can resolve fluctuations with frequencies up to 10 kHz (Nyquist criterion). The higher energy content (due to more resolved frequencies) of the experimental data leads to more activity in the velocity signal as depicted in Fig. 11. Nevertheless, a good quantitative agreement between the signals can be seen. Applying a low-pass filter at 800 Hz on the numerical and hot-wire probes matches the amplitudes of the velocity signals. Nevertheless, filtering the signals have a negligible effect on the agreement of the turbulence intensity and length scale of the numerical and experimental data (not shown). Thus, the signals are not additionally low-pass filtered in the following. The evaluated turbulence intensity and integral length scale along the centerline for the fine case, recycled case, and two experimental measurements (EXP) are depicted in Figs. 12 and 13 for the VG and ATG, respectively. Absolute values are not discussed here because the results are shown derived from the effective velocity v_{eff} for comparison purposes only.

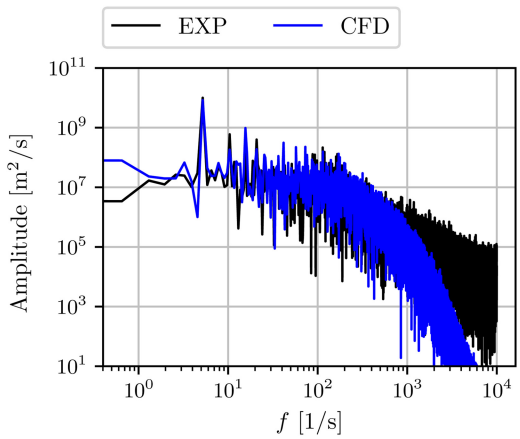

Fig. 10 VG: frequency spectrum of probe signals downstream of the generator at $x/\tilde{L}_p = 1$. CFD (fine) data converted to v_{eff}.

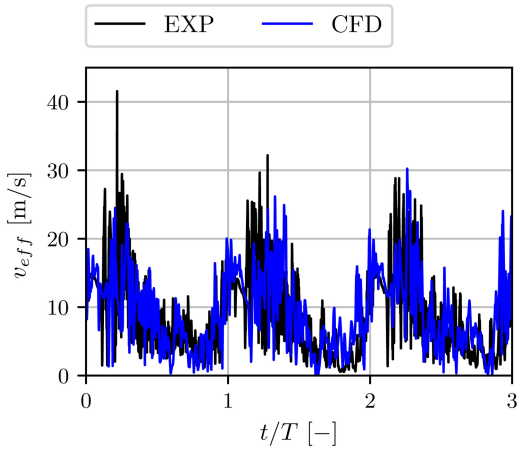

Fig. 11 VG: unfiltered probe signals downstream of the generator at $x/\tilde{L}_p = 1$. CFD (fine) data converted to v_{eff}.

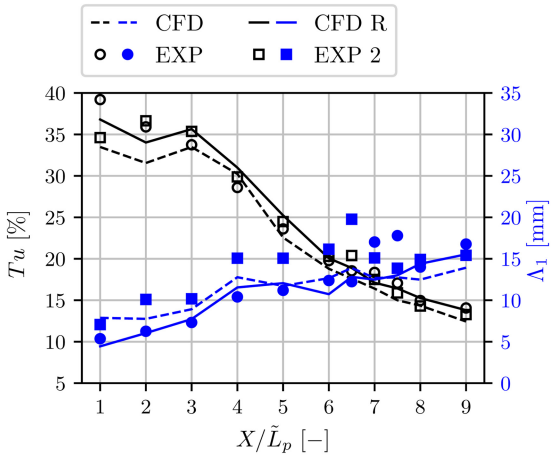

Fig. 12 VG: comparison of turbulence intensity *Tu* and integral length scale Λ_1 at the centerline. CFD used the fine mesh and CFD R corresponds to the recycled case.

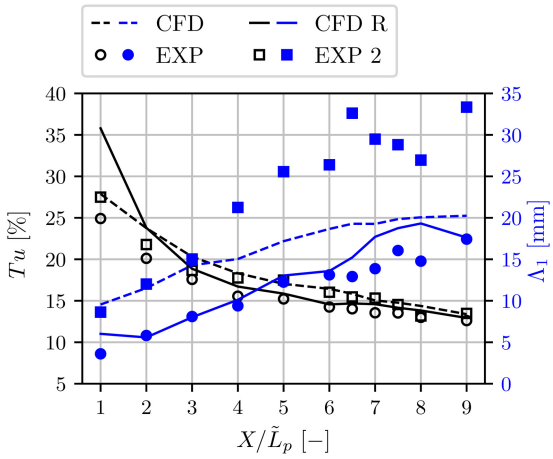

Fig. 13 ATG: comparison of turbulence intensity *Tu* and integral length scale Λ_1 at the centerline. CFD used the medium mesh and CFD R corresponds to the recycled case.

Downloaded from http://asmedigitalcollection.asme.org/turbomachinery/article-pdf/144/11/111003/6896975/turbo_144_11_111003.pdf by Universitat Der Bundeswehr Munchen user on 08 August 2023

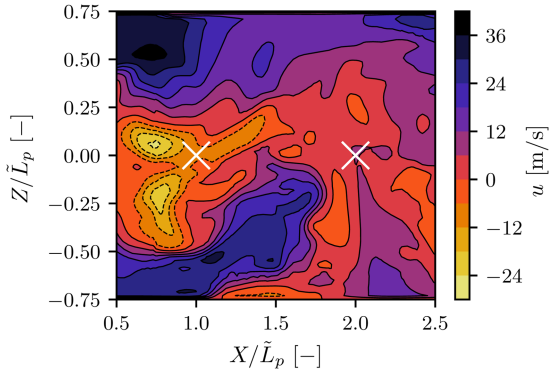

Fig. 14 VG: instantaneous axial velocity downstream of the vortex generator in the centerline. Probe locations are marked with a cross.

First, the trend for the vortex generator is discussed. One can see decaying turbulence intensity downstream of the vortex generator. At $X/\tilde{L}_p = 2$, the turbulence intensity Tu shows a kink. It is a result of applying Eq. (4) onto the LES velocity signal. There is no kink when the directionally sensitive velocity components (u, v, w) are evaluated instead of the effective velocity component v_{eff} (Figs. 16 and 17). This implies that the pitch factors to weight the influence of the velocity components (Eq. (4)) may need to be adjusted just downstream of the vortex generator to correctly determine v_{eff}. It may also indicate that the experimental data are inaccurate at those locations because of the proximity to a recirculation zone shown in Fig. 14. With respect to the turbulence length scale, the two experimental datasets differ by around 5 mm (0.2 in.) at most locations indicating the difficulty of reproducing the length scale. The predicted length scales match well with the experimental scales. Second, the validation of the ATG results are discussed in Fig. 17. The turbulence intensity matches well with the experiment. However, just downstream of the active turbulence grid, the results of the recycled CFD predict a turbulence intensity which is around 10% higher than the experimental data. As mentioned before, this discrepancy may arise from the sensitivity of the used pitch factors to determine the effective velocity v_{eff} in the proximity of a recirculation zone or the uncertainty of the probe placing. Concerning the integral length scale, the experimental data show difficulty of reproduction once more. The CFD case (here medium mesh) has an offset of 5 mm (0.2 in.) with respect to the higher resolved recycled case as was also shown in the mesh study for the VG case (Fig. 9). There is an almost exact agreement between the recycled trend of the integral length scale and one of the experimental results. All in all, the simulations clearly show the correct trend suggesting that the numerical approach works using complex meshes with moving sections or the recycling approach.

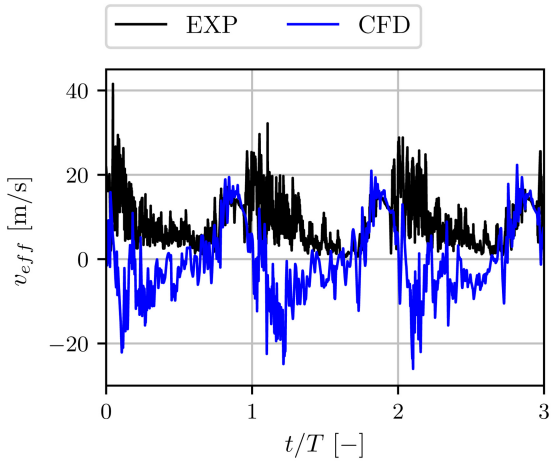

Fig. 15 VG: unfiltered probe signals downstream of the plate at $x/\tilde{L}_p = 1$. CFD (fine) data show the axial velocity component u.

7 Results

In the previous section, the numerical data were converted to the effective velocity v_{eff} which was measured by the 1D hot-wire probe. This way the numerical probe signal is insensitive to the flow direction. In the following, the computed velocity components u, v, and w are used directly to obtain the turbulence intensity and integral length scales. The turbulence parameters are evaluated once more along the centerline. The integral length scale is derived from the two-point and one-point approaches and the differences are discussed. Finally, the turbulence parameters can be discussed just upstream of the film cooling test section in a 2D plane ranging from the wall from which the film cooling is injected to the center of the channel.

8 Turbulence Intensity Along Centerline

Figure 14 shows the contour of the instantaneous axial velocity u downstream of the vortex generator's plate in the axial (X) and vertical (Z) planes. The numerical probe points are marked with a cross. It is visible that the axial velocity component in the vicinity of a probe has a negative sign indicating that directional sensitivity is of importance. Figures 16 and 17 show the isotropic turbulence intensities Tu (Eq. (8)) for both active turbulence generators. In the vicinity of the vortex generator $X/\tilde{L}_p < 4$, there is a high deviation between directionally sensitive and insensitive (using v_{eff} from Eq. (4)) turbulence intensities as shown in Fig. 16. The directionally sensitive turbulence intensities are up to 300% just downstream of the plate. This is due to the fact that a directionally sensitive mean velocity signal fluctuates around zero and the effective velocity (v_{eff}) does not (see Fig. 15). Further downstream of the plate $X/\tilde{L}_p > 4$, there are no more zero crossings of the velocity signal and near the film cooling test section at $X/\tilde{L}_p \approx 7$, the turbulence intensity of the pure u-component and v_{eff} matches well. This indicates isotropic turbulence (at the centerline) and that the hot-wire is able to measure the correct values of $Tu_u = Tu_{v_{\text{eff}}} = 17.5\%$ at the location of the film cooling test section. With respect to the ATG (Fig. 17), the turbulence intensity in the mainstream direction u is lower just downstream of the generator compared to the VG. The velocity signal only occasionally has zero crossings at $X/\tilde{L}_p = 1$ (not shown) so that $Tu_u = Tu_{v_{\text{eff}}}$ at $X/\tilde{L}_p \geq 1$. The turbulence intensity decays from around $Tu_u = 40\%$ to around 15% at the film cooling test section. The turbulence created by the ATG is anisotropic in the centerline because the turbulence intensities in the Y and Z directions are around $Tu_{v,w} = 12\%$ showing a constant offset in the centerline of 3% to Tu_u.

8.1 Turbulence Length Scale Along Centerline. So far the integral length scale was determined at one axial location using one probe (Λ_1) and applying the Taylor's hypothesis which may not be valid at the high turbulence intensity conditions. Hence, the two-point approach (Λ_2) was presented (Eq. (13)) in the post-processing sections as well. In the CFD domain, probes are spaced one cell apart in each direction. This allows to determine the integral length scale in each direction (X, Y, Z). First, the trend of the integral length scale along the centerline is discussed for the VG (Fig. 18). The one-point approach for the determination of Λ_1 can only be applied in the axial direction (X) because it is in line with the main flow direction which is needed for the application of Taylor's hypothesis. One can see that for $X/\tilde{L}_p \geq 4$, the one- and two-point methods lead to the same result and a length scale of $\Lambda_2 = 15$ mm (0.6 in.) at the test section. There is a small deviation at $X/\tilde{L}_p = 7$ which may arise from the resolution

Downloaded from http://asmedigitalcollection.asme.org/turbomachinery/article-pdf/144/11/111003/6896975/turbo_144_11_111003.pdf by Universitat Der Bundeswehr Munchen user on 08 August 2023

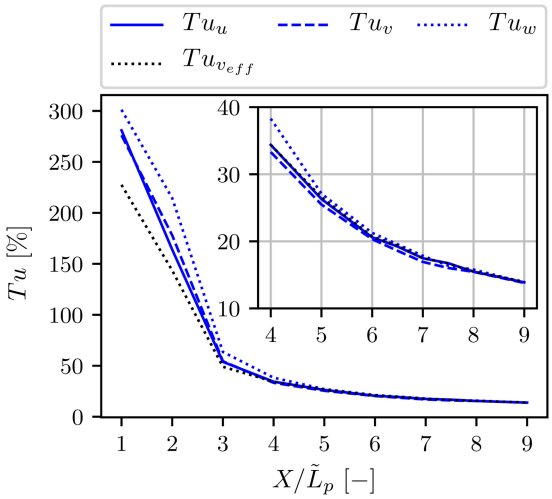

Fig. 16 VG: turbulence intensity *Tu* along the centerline depending on the velocity vector component

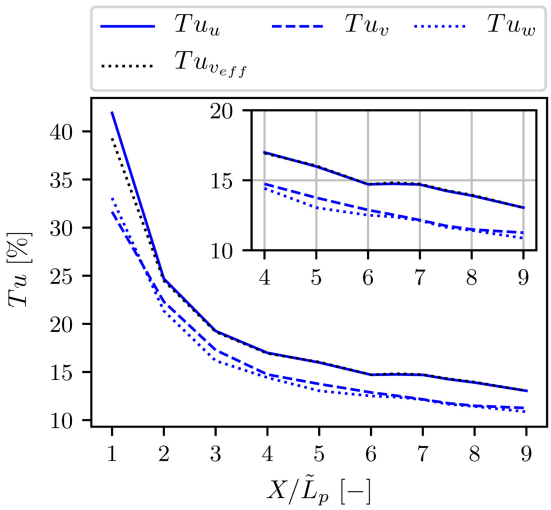

Fig. 17 ATG: turbulence intensity *Tu* along the centerline depending on the velocity vector component

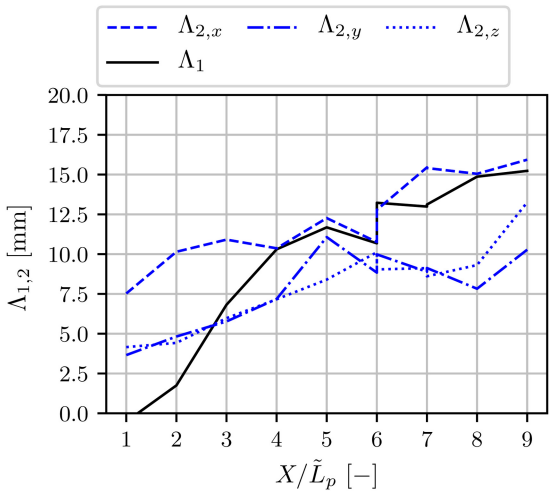

Fig. 18 VG: integral length scale Λ_1 (one-point approach) and spatial determined integral length scales Λ_2 along the centerline

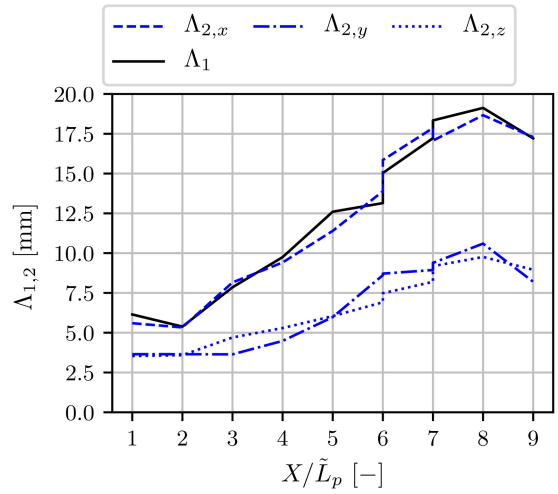

Fig. 19 ATG: integral length scale Λ_1 (one-point approach) and spatial determined integral length scales Λ_2 along the centerline

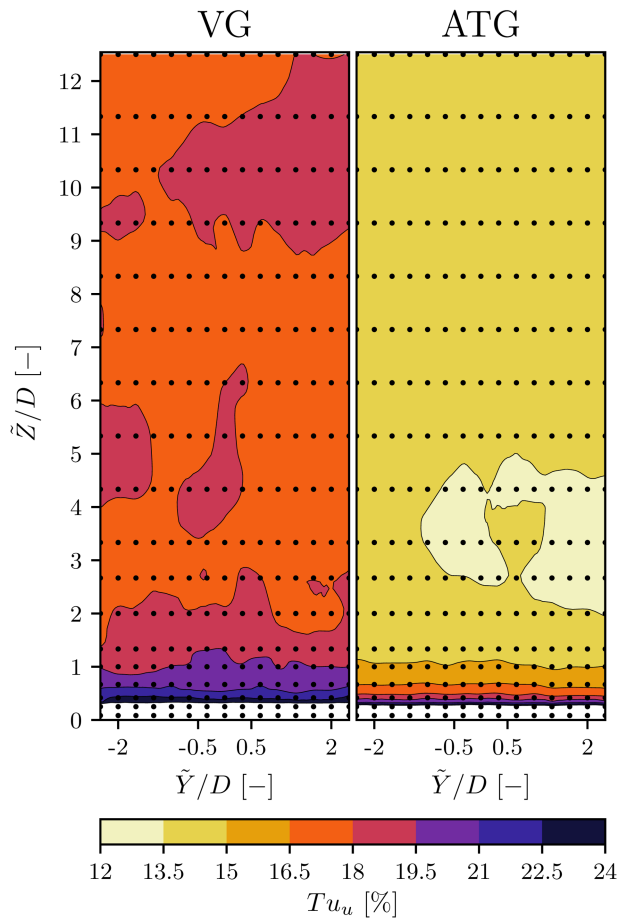

Fig. 20 Contour of the turbulence intensity *Tu* upstream of the film cooling section at $X/\tilde{L}_p = 7$. Probe locations are marked by black dots.

of the spatial probe points which influence the integral of the correlation function $R_{V'V'}(\vec{x_0}, \Delta x)$. Hence, the Taylor's hypothesis works in this case even for high turbulence regions up to 35% (compare Fig. 16). Just downstream of the rotating plate, the time average velocity of the axial component u has a negative sign (compared with Fig. 15). Hence, the integral length scale

Downloaded from http://asmedigitalcollection.asme.org/turbomachinery/article-pdf/144/11/111003/6896975/turbo_144_11_111003.pdf by Universitat Der Bundeswehr Munchen user on 08 August 2023

(Λ_1) which is the product of the integral time scale and $\overline{u}$ evaluates below zero (Eq. (11)). In the downstream region $X/\tilde{L}_p < 4$, the velocity component u continues to have sign changes (not shown) which influences the time average velocity $\overline{u}$ so that the value of Λ_1 remains inaccurate. The length scales in the Y and Z directions are equally smaller than the scales in the main flow direction with a size of around 7.5 mm (0.3 in.). This indicates anisotropic turbulence scales. Next, the trend is discussed for the ATG in Fig. 19. As mentioned before, the flow field differs between the ATG and VG. There is no strong recirculation zone downstream of the turbulence generator so that $\Lambda_1 = \Lambda_{2,x}$ for all points along the centerline. The sizes of the length scales are of a similar order than for the VG and the scales are also anisotropic along the centerline. There is an anisotropy of a factor 2 between the lateral and the axial length scales. In a lean burn single-section combustors, a factor of 4 was found between axial and circumferential integral time scales [11].

8.2 Turbulence Parameters at the Film Cooling Test Section. Additionally, data of 270 probes are used to visualize the turbulence quantities upstream of the film cooling test section at $X/\tilde{L}_p = 7$. Figure 20 depicts the isotropic turbulence intensity Tu_u for the VG and the ATG. The data are shown in a plane which is non-dimensionalized by the film cooling hole diameter $D = 6$ mm (0.24 in.). The plane ranges from the wall $\tilde{Z}/D = 0$ to the center of the test section $\tilde{Z}/D = 12.5$ (equals $Z/\tilde{L}_p = 0$). Moreover, the plane resolves the lateral range between $\tilde{Y}/D \pm 2.33$. For reference, the film cooling jet would enter the test section between $\tilde{Y}/D \pm 0.5$. The turbulence intensity in both planes is more or less homogeneous and varies only by around 3% from the center of the channel to the near-wall region at around $\tilde{Z}/D = 1$. Below $\tilde{Z}/D = 0.5$, the turbulence intensity Tu_u is increasing up to 48% due to actually higher average velocity fluctuations (u_{rms}) near the wall and due to decreasing average velocity (not shown). Increased turbulence intensities near the wall were also visible in an experimental combustor simulator [17]. The turbulence intensity for Tu_v and Tu_w in the plane is of the same order of magnitude but has different structures and hence indicates anisotropy (not shown). All in all, the vortex generator produces an anisotropic turbulence intensity of around 17.5% which is around 2.5% higher than the active turbulence generator as was also predicted in Figs. 16 and 17.

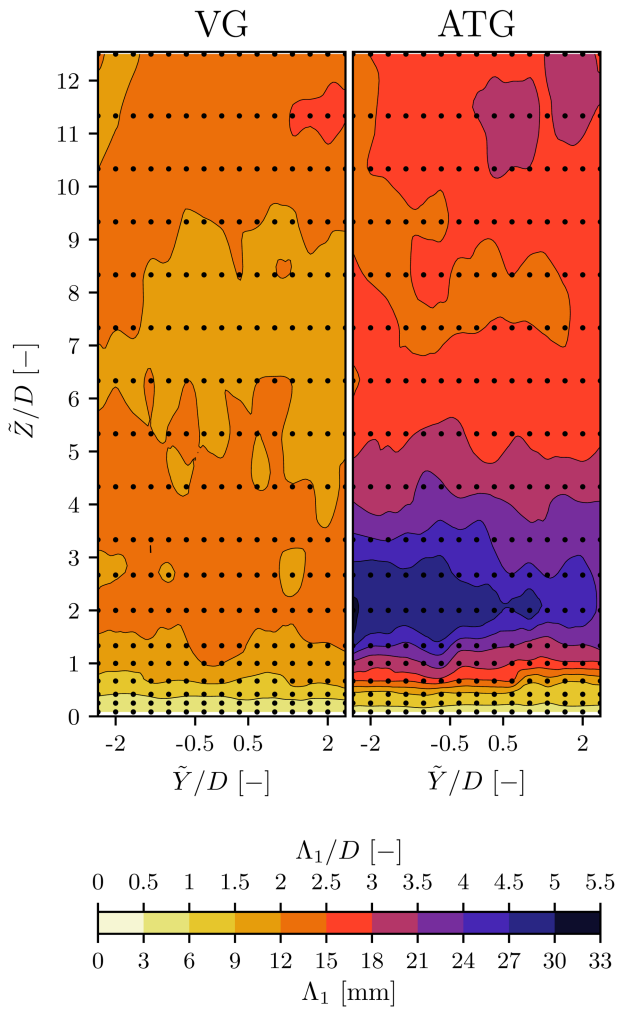

Fig. 21 Contour of the integral length scale Λ_1 upstream of the film cooling section at $X/\tilde{L}_p = 7$. Probe locations are marked by black dots.

Figure 21 shows the integral length scale Λ_1 in the plane upstream of the film cooling test section. The one-point approach leads to the same result as the two-point approach at the centerplane, thus $\Lambda_1 \approx \Lambda_{2,x}$ is assumed in this plane. The length scale is given in absolute values (mm) and also non-dimensionalized by the film cooling hole diameter. The length scale for the VG in this plane varies between 9 and 15 mm and starts to decrease near the wall. The distribution of the length scale created by the ATG differs from the VG distribution. In general, higher length scales between 15 and 30 mm are visible. In contrast to the VG field, there is an increase of the length scale up to 33 mm ($\Lambda_1/D \approx 5D$) in a near wall region from $\tilde{Z}/D = 1 - 5$ which differs by factor 2 of the value from the center of the test section. Large-scale turbulence $\Lambda_1/D \approx 3$ is believed to be characteristically for gas turbines [39]. The high values result from high integral time scales (not shown) and is no result of the time-averaged velocity field. The flow field generated by the ATG shows a slight asymmetric distribution of the length scale near the film cooling injection. This may result from the sensitivity of the integration limit for the correlation coefficient.

9 Conclusion

To investigate the future film cooling simulations under the influence of more realistic crossflow conditions, turbulence generators were setup in a wind tunnel. The so-called vortex generator (VG) consists of one shaft with a rotating plate. The ATG comprises several shafts and wings. For both generators, CFD cases involving moving meshes were created. Moreover, simple meshes with no moving domains but higher mesh resolution were created. Here, the sampled velocity field downstream of the turbulence generators from CFD simulations with moving meshes were reused (recycled) and led to excellent results. To determine the turbulence boundary conditions for the film cooling test rig, numerical and experimental probe signals were evaluated. The numerical point probe data were converted to the hot-wire velocity signal v_{eff}. This way the LES could be validated by the experimental data. The turbulence intensity and integral length scale were determined from the probe signals downstream of the vortex generator. The triple decomposition was applied on to the signals in order that the fluctuating velocity V' component incorporates only the stochastic component (and not the periodic one as well). The determination of the turbulence intensity Tu indicated isotropic and anisotropic turbulence intensities in the centerline for the VG and ATG, respectively. The intensities were $Tu = 17.5\%$ and 15% at the inlet of the film cooling test section ($X/\tilde{L}_p = 7$), respectively. Two methods were applied to determine the turbulence length scales downstream of the generators. The one-point two times approach could be applied to both the experimental and numerical data. The two-point one time approach using spatial integration of the probe signals from the LES simulation does not require the application of Taylor's hypothesis.

Downloaded from http://asmedigitalcollection.asme.org/turbomachinery/article-pdf/144/11/111003/6896975/turbo_144_11_111003.pdf by Universitat Der Bundeswehr Munchen user on 08 August 2023

Both generators created anisotropic length scales in which the lateral components were approximately 2× smaller than the axial component. The one-point method leads to the exact same length scales as the two-point method in regions of the flow field in which the velocity signal has no zero-crossing. This is of interest because in real combustor experiments, the application of the two-point method is difficult. However, attention has to be paid with the one-point method and directionally sensitive data near recirculation zones. The turbulence parameters were evaluated in a 2D plane at the film cooling test section to evaluate the near-wall region in which the coolant injection occurs. The turbulence intensity increases by 5–22.5% (VG) and 20% (ATG) near the wall and below a height of $\tilde{Z}/D = 0.5$ to 45%. The turbulence length scale for the VG remains nearly constant $\Lambda_1/D \approx 2$ from the center to the near-wall region. This differs from the turbulence field generated by ATG in which the length scale increases in a near wall region. The size of turbulence length scales is in the range of $\Lambda_1/D \approx 0.5 - 5.5$. All in all, both active turbulence generators create a unique flow field which provide combustor-like turbulence quantities at the inlet of the film cooling test section. This allows for film cooling investigations with realistic inflow conditions.

Acknowledgment

We would like to thank our former students Sebastian Privik and Leonhard Englaender for carrying out the majority of the 1D hot-wire measurements. We thank Prof. Dr. Ing. Kilian Oberleithner from Technische Universität Berlin Laboratory for Flow Instabilities and Dynamics for discussing the two-point at one time approach. Moreover, we thank Dr. Roderick Lubbock from Imperial College Dept. Aeronautics for discussing turbulence measurements at gas turbine combustor exits. The work is sponsored by the Deutsche Forschungsgemeinschaft (DFG project number PF 443/7-1). Moreover, we acknowledge financial support by Universität der Bundeswehr München. The support is gratefully acknowledged.

Conflict of Interest

There are no conflicts of interest.

Data Availability Statement

The authors attest that all data for this study are included in the paper.

Nomenclature

f = frequency (1/s)
r = plate coordinate (m)
t = time (s)
D = film cooling hole diameter (mm)
T = period length of the signal (s)
V = any velocity component (m/s)
v_{eff} = effective hot-wire velocity (m/s)
v_{wall} = velocity at the wall of a wing (m/s)
L_p = plate length (mm)
$\tilde{L}_p$ = rounded plate length (mm)
$R_{V'V'}$ = correlation coefficient
V_{rms} = average velocity fluctuation (m/s)
V' = velocity fluctuation (m/s)
V'_s = stochastic velocity fluctuation (m/s)
V'_p = periodic velocity fluctuation (m/s)
h, k = pitch factors to convert signal
u, v, w = velocity components (m/s)
Tu = turbulence intensity (%)
X, Y, Z = Cartesian coordinates (m)

Greek Symbols

Λ_τ = integral time scale using one probe (s)
Λ_1 = integral length scale using one probe (mm)
Λ_2 = integral length scale using several probes (mm)
τ = time lag (s)
ϕ = phase angle
ω = rotational speed (1/s)

References

[1] Idowu Oguntade, H., Burns, A. D., and Pourkashanian, M., 2013, "Improved Trench Film Cooling With Shaped Trench Outlets," ASME J. Turbomach., **135**(2), p. 021009.
[2] Zhang, W., Zhou, S., Wu, Z., Li, G., and Kou, Z., 2019, "Film Cooling Mechanism of Combined Hole and Saw-Tooth Slot," Int. J. Turbo Jet-Engines, **36**(4), p. 9.
[3] Sperling, S., Christensen, L., Celestina, R., Mathison, R., Aksoy, H., Liu, J., and Nickol, J., 2021, "Coupling of Mainstream Velocity Fluctuations With Plenum Fed Film Cooling Jets," Turbo Expo: Power for Land, Sea, and Air, Vol. 84973, Virtual, Online, June 7–11, American Society of Mechanical Engineers, p. 14.
[4] Kalghatgi, P., and Acharya, S., 2014, "Modal Analysis of Inclined Film Cooling Jet Flow," J. Turbomach., **136**(8), p. 11.
[5] Hou, R., Wen, F., Luo, Y., Tang, X., and Wang, S., 2019, "Large Eddy Simulation of Film Cooling Flow From Round and Trenched Holes," Int. J. Heat Mass Transfer, **144**, p. 13.
[6] Zamiri, A., You, S. J., and Chung, J. T., 2020, "Large Eddy Simulation of Unsteady Turbulent Flow Structures and Film-Cooling Effectiveness in a Laidback Fan-Shaped Hole," Aerospace Sci. Technol., **100**, p. 16.
[7] Lubbock, R., and Oldfield, M., 2018, "Turbulent Velocity and Pressure Fluctuations in Gas Turbine Combustor Exit Flows," Proc. Inst. Mech. Eng. Part A: J. Power Energy, **232**(4), pp. 337–349.
[8] Driscoll, J., and Pelaccio, D., 1978, "Laser Velocimetry Measurements in a Gas Turbine Research Combustor," Laser Velocimetry and Particle Sizing; Third International Workshop, West Lafayette, IN, pp. 158–165.
[9] Folk, M., Miller, R. J., and Coull, J. D., 2020, "The Impact of Combustor Turbulence on Turbine Loss Mechanisms," ASME J. Turbomach., **142**(9), p. 091009.
[10] Hassa, C., Voigt, L., Schroll, M., Heinze, J., Willert, C., and Bagchi, I., 2018, "Optische Messung von Geschwindigkeit und Temperatur am Austritt einer Magerbrennkammer unter realistischen Betriebsbedingungen," Deutscher Luft- und Raumfahrtkongress, Friedrichshafen, Germany, Sept. 4–6, Deutsche Gesellschaft für Luft-und Raumfahrt-Lilienthal-Oberth e.V., p. 10.
[11] Willert, C., Schroll, M., Heinze, J., and Soworka, T., 2019, "High-Speed PIV at the Exit of a Lean-Burn Combustion Chamber Operated at Elevated Pressure," 13th International Symposium on Particle Image Velocimetry – ISPIV 2019, Munich, Germany, July 22–24, p. 11.
[12] Lenzi, T., Palanti, L., Picchi, A., Bacci, T., Mazzei, L., Andreini, A., and Facchini, B., 2020, "Time-Resolved Flow Field Analysis of Effusion Cooling System With Representative Swirling Main Flow," ASME J. Turbomach., **142**(6), p. 061008.
[13] Lenzi, T., Picchi, A., Andreini, A., and Facchini, B., 2022, "Analysis of Swirl Number Effects on Effusion Flow Behaviour Using Time Resolved PIV," ASME J. Turbomach., **144**(8), p. 081001.
[14] Dullenkopf, K., and Mayle, R. E., 1994, "An Account of Free-Stream-Turbulence Length Scale on Laminar Heat Transfer," Turbo Expo: Power for Land, Sea, and Air, Volume 4: Heat Transfer; Electric Power; Industrial and Cogeneration, The Hague, The Netherlands, June 13–16, American Society of Mechanical Engineers, Vol. 78866, p. 6.
[15] Gifford, A. R., Diller, T. E., and Vlachos, P. P., 2009, "An Investigation of the Physical Mechanism of Heat Transfer Augmentation in Stagnating Flows Subject to Freestream Turbulence," Turbo Expo: Power for Land, Sea, and Air, Jacksonville, FL, Aug. 10–14, Vol. 48470, ASMEDC, pp. 575–584.
[16] Moss, R. W., 1992, "The Effects of Turbulence Length Scale on Heat Transfer," PhD thesis, University of Oxford, Oxford.
[17] Barringer, M. D., Richard, O. T., Walter, J. P., and Thole, K. A., 2002, "Flow Field Simulations of a Gas Turbine Combustor," ASME J. Turbomach., **124**(3), pp. 508–516.
[18] Cha, C. M., Ireland, P. T., Denman, P. A., and Savarianandam, V., 2013, "Turbulence Levels Are High at the Combustor-Turbine Interface," Turbo Expo: Power for Land, Sea, and Air, Copenhagen, Denmark, June 11–15, American Society of Mechanical Engineers, Vol. 44748, p. 20.
[19] Bacci, T., Facchini, B., Picchi, A., Tarchi, L., Koupper, C., and Champion, J.-L., 2015, "Turbulence Field Measurements at the Exit of a Combustor Simulator Dedicated to Hot Streaks Generation," Heat Transfer, Vol. 5C, Montreal, Quebec, Canada, June 15–19, American Society of Mechanical Engineers, p. 14.
[20] Koupper, C., Gicquel, L., Duchaine, F., Bacci, T., Facchini, B., Picchi, A., Tarchi, L., and Bonneau, G., 2016, "Experimental and Numerical Calculation of Turbulent Timescales at the Exit of an Engine Representative Combustor Simulator," ASME J. Eng. Gas Turbines Power, **138**(2), p. 021503.
[21] Schroll, M., Doll, U., Stockhausen, G., Meier, U., Willert, C., Hassa, C., and Bagchi, I., 2017, "Flow Field Characterization at the Outlet of a Lean Burn Single-Sector Combustor by Laser-Optical Methods," ASME J. Eng. Gas Turbines Power, **139**(1), p. 011503.

Downloaded from http://asmedigitalcollection.asme.org/turbomachinery/article-pdf/144/11/111003/6896975/turbo_144_11_111003.pdf by Universitat Der Bundeswehr Munchen user on 08 August 2023

[22] Straußwald, M., Schmid, K., Müller, H., and Pfitzner, M., 2017, "Experimental and Numerical Investigation of Turbulent Mixing in Film Cooling Applications," Turbo Expo: Power for Land, Sea, and Air, Volume 5C: Heat Transfer, Charlotte, NC, June 26–30, Vol. 50893, American Society of Mechanical Engineers, p. 13.
[23] Schreivogel, P., Kröss, B., and Pfitzner, M., 2014, "Density Ratio Effects on the Flow Field Emanating From Cylindrical Effusion and Trenched Film Cooling Holes," Turbo Expo: Power for Land, Sea, and Air, Heat Transfer, Vol. 5B, Düsseldorf, Germany, June 16–20, American Society of Mechanical Engineers, Vol. 45721, p. 13.
[24] Straußwald, M., Sander, T., Bakhtiari, A., and Pfitzner, M., 2018, "High-Speed Velocity Measurements of Film Cooling Applications at High-Turbulence Main Flow Conditions," Turbo Expo: Power for Land, Sea, and Air, Vol. 51104, Oslo, Norway, June 11–15, American Society of Mechanical Engineers, p. 10.
[25] Straußwald, M., Abram, C., Sander, T., Beyrau, F., and Pfitzner, M., 2021, "Time-Resolved Temperature and Velocity Field Measurements in Gas Turbine Film Cooling Flows With Mainstream Turbulence," Exp. Fluids, **62**(1), p. 17.
[26] Bakhtiari, A., Sander, T., Straußwald, M., and Pfitzner, M., 2018, "Active Turbulence Generation for Film Cooling Investigations," Turbo Expo: Power for Land, Sea, and Air, Vol. 51104, Oslo, Norway, June 11–15, American Society of Mechanical Engineers, Vol. 51104, p. 11.
[27] Makita, H., 1991, "Realization of a Large-Scale Turbulence Field in a Small Wind Tunnel," Fluid Dyn. Res., **8**(1), pp. 53–64.
[28] Makita, H., and Sassa, K., 1991, "Active Turbulence Generation in a Laboratory Wind Tunnel," *Advances in Turbulence 3*, Johansson, A. V., and Alfredsson, P. H., eds., Springer, Berlin, pp. 497–505.
[29] Bruun, H. H., 1995, *Hot-Wire Anemometry Principles and Signal Analysis*, Vol. 1, Oxford University Press Inc., New York.
[30] Oguntade, H. I., Andrews, G. E., Burns, A., Ingham, D., and Pourkashanian, M., 2010, "CFD Predictions of Single Row Film Cooling With Inclined Holes: Influence of Hole Outlet Geometry," Proceedings of ASME Turbo Expo 2010: Power for Land, Sea and Air, Glasgow, UK, June 14–18, Vol. 43994, p. 15.
[31] Thomas, M., Duchaine, F., Gicquel, L., and Koupper, C., 2018, "Impact of Realistic Inlet Condition on LES Predictions of Isolated High Pressure Vanes," 12th International ERCOFTAC Symposium on Engineering Turbulence Modelling and Measurements, Sept. 26–28, p. 6.
[32] Tropea, C., Yarin, A., and Foss, J. F., 2007, *Handbook of Experimental Fluid Mechanics*, Springer-Verlag, Berlin.
[33] Reynolds, W. C., and Hussain, A. K. M. F., 1972, "The Mechanics of an Organized Wave in Turbulent Shear Flow. Part 3. Theoretical Models and Comparisons With Experiments," J. Fluid Mech., **54**(2), pp. 263–288.
[34] Baj, P., Bruce, P. J. K., and Buxton, O. R. H., 2015, "The Triple Decomposition of a Fluctuating Velocity Field in a Multiscale Flow," Phys. Fluids, **27**(7), p. 25.
[35] Nieuwstadt, F. T., Boersma, B. J., and Westerweek, J., 2016, *Introduction to Theory and Applications of Turbulent Flows*, 1st ed., Springer International Publishing, Cham, Germany.
[36] Pope, S. B., 2010, *Turbulent Flows*, 7th ed., Cambridge University Press, Cambridge, UK.
[37] Comte-Bellot, G., and Corrsin, S., 1971, "Simple Eulerian Time Correlation of Full- and Narrow-Band Velocity Signals in Grid-Generated, 'Isotropic' Turbulence," J. Fluid Mech., **48**(2), pp. 273–337.
[38] Keating, A., Piomelli, U., Balaras, E., and Kaltenbach, H.-J., 2004, "*A Priori* and *a Posteriori* Tests of Inflow Conditions for Large-Eddy Simulation," Phys. Fluids, **16**(12), pp. 4696–4712.
[39] Schmidt, D. L., and Bogard, D. G., 1996, "Effects of Free-Stream Turbulence and Surface Roughness on Film Cooling," Turbo Expo: Power for Land, Sea, and Air Vol. 4 Heat Transfer; Electric Power; Industrial and Cogeneration, Birmingham, UK, June 10–13, American Society of Mechanical Engineers, Vol. 78750, p. 7.

Downloaded from http://asmedigitalcollection.asme.org/turbomachinery/article-pdf/144/11/111003/6896975/turbo_144_11_111003.pdf by Universitat Der Bundeswehr Munchen user on 08 August 2023